CRYSTAL GROWTH & DESIGN

pubs.acs.org/crystal

Article

Heat-Mediated Micro- and Nano-pore Evolution in Sea Urchin Biominerals

Marie Albéric,* Emil Zolotoyabko, Oliver Spaeker, Chenghao Li, Maryam Tadayon, Clemens N.Z. Schmitt, Yael Politi, Luca Bertinetti, and Peter Fratzl*

Cite This: *Cryst. Growth Des.* 2022, 22, 3727−3739

Read Online

ACCESS | Metrics & More | Article Recommendations | Supporting Information

ABSTRACT: Biomineralized structures with intricate shapes and morphologies, such as sea urchin skeletal elements, grow via the deposition of hydrated amorphous calcium carbonate (ACC) particles that subsequently crystallizes into single-crystalline calcite. This process is accompanied by volume changes due to density differences between the initial and final mineral state as well as variations in hydration levels. For this reason, the presence of macroporosity in synthetic systems was shown to be pivotal in the formation of large single crystals through ACC precursors. However, the role of macroporosity down to nanoporosity in the formation of biogenic minerals remains unknown. Here, we investigate the micro- and nano-porosity as well as the evolution of internal interfaces in the spines and test plates of *Paracentrotus lividus* sea urchins during the heat-mediated crystallization of remnant ACC and the destruction of intracrystalline organic molecules, using SEM, FIB-SEM, and *in situ* heating synchrotron SAXS measurements. We show the presence of nanopores likely filled with hydrated organics and visualize the evolution of nano- to micro-pores induced by heating, which may serve to accommodate the volume changes between amorphous and crystalline phases. The obtained results analyzed using thermodynamical considerations suggest that the growth in size of the nanopores is controlled by Ostwald ripening and is well described in the framework of classical pore coarsening theories. The extracted activation energies manifest that nanopore coarsening in the test plates is governed by surface diffusion, whereas in the spines by bulk diffusion. We suggest that such striking differences in diffusion mechanisms are caused by dissimilar levels of macroporosity and distributions of nano- and micro-internal interfaces in pristine biominerals.

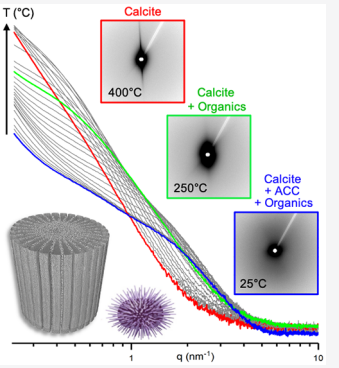

1. INTRODUCTION

Inspired by the unique morphologies as well as the exceptional mechanical and optical properties of echinoderm biominerals, novel concepts toward the design of artificial materials are under intensive development for various applications. For example, by replicating the macrostructure of sea urchin skeletal plates, porous solids with interconnected pores of well controlled sizes and shapes,[1,2] as well as single crystals with complex morphologies[3,4] were produced for potential prosthetic biomaterials, lightweight structural ceramics, and catalyst supports. Micropatterned single crystals and microlens arrays, which are crucial components in electronic, sensory, and optical devices, were fabricated by mimicking the brittle star arms,[5−8] and elastic cements were developed inspired from the nanostructure of sea urchin spines.[9]

The morphology of echinoderm skeletal calcitic ossicles is characterized by a macroporous, three-dimensional arrangement of mineralized trabeculae called stereom. During the animal's lifetime, the stereom macropores are filled with organic tissues containing different cell types.[10,11] These particular lightweight structures reveal interesting mechanical characteristics, such as limiting crack propagation in the sea urchin test plates[12] and spines.[13] In the case of the *Ophiocoma wendtii* brittle star arms, the stereom "extends into a regular array of spherical microstructures" that were suggested to have optical functions.[14,15]

Despite the complicated macromorphology of the stereom structure, echinoderm skeletal ossicles in the form of a few millimeter-wide plates or centimeter-long spines behave as single crystals of calcite when observed under polarized light microscopy[16] or analyzed using X-ray and electron diffraction techniques.[17−19] To understand the origin of this intriguing characteristic, numerous research groups studied the mechanisms controlling the *in vivo* and *in vitro* formation of large single crystals of calcite with complex morphologies. Three main findings in this field can be formulated as follows: (i) deposition of an amorphous calcium carbonate (ACC) phase prior to crystallization (for review, see refs 20−22); (ii) preferential interaction of some organic molecules with specific crystal

Received: January 20, 2022
Revised: April 13, 2022
Published: April 29, 2022

https://doi.org/10.1021/acs.cgd.2c00083
Cryst. Growth Des. 2022, 22, 3727−3739

planes guiding crystal growth (for review, see refs 23, 24); and (iii) presence of organic templates imposing crystal shapes (for review, see ref 25).

Biomineralization pathways involving the crystallization of ACC phases imply a substantial volume change and mass transport[26] once ACC crystallized, e.g., into calcite due to the differences in the volumetric mass densities of hydrated ACC (2.28 g/cm^3 for $CaCO_3{\cdot}H_2O$), anhydrous ACC (2.43 g/cm^3 for $CaCO_3{\cdot}0.5H_2O$), and calcite (2.71 g/cm^3).[27] Inspired by the stereom macrostructure, Aizenberg et al.[5] showed that patterning a surface with carefully placed PDMS slabs (i.e., 3 μm in size, with 8 μm spacing) allows an ACC film to transform into millimeter-sized single crystals of calcite once an imprinted nanoregion of self-assembled monolayers is used as a nucleation site. Based on this seminal study, a kinetic model built on thermodynamic considerations showed that the structural features of the macropatterned ACC template (slab thickness, size, and spacing between pores) can control the crystal nucleation process and thus the probability of obtaining large and porous single crystals of calcite.[26] These works draw a link between macroporosity and the crystallization mechanisms of ACC into calcite. The crystallization of ACC in confinement was further studied *in vitro* in diverse systems, such as porous polycarbonate track-etched membranes,[28] via polymer-induced liquid-precursor processes,[29,30] liposomes,[31,32] microfluidic devices,[33,34] and microfluidic droplets.[35,36]

Therefore, it appears that the presence of macropores with specific characteristics play an important role in accommodating volume changes during ACC crystallization toward *in vitro* growth of large single crystals. In order to further investigate the role of porosity in biomineralization processes, we study here the nanometer and micrometer structural reorganization occurring during the heat-induced crystallization of biogenic ACC, initially trapped within *Paracentrotus lividus* sea urchin skeletal elements that present different levels of macroporosity. We propose to do so by taking advantage of the unique characteristic of sea urchin biominerals, i.e., the presence of remnant anhydrous ACC in their mineralized structures.[37−39] Indeed, adult sea urchin skeletal elements, in particular the spines, were shown to form via hydrated ACC nanoparticles[40] that later crystallize into calcite through anhydrous ACC[41] as first evidenced in sea urchin larval spicule.[42,43] In addition, organic macromolecules are entrapped within the calcite lattice during crystal growth.[37,38,44−50] Consequently, nanoinclusions of ACC and/or macromolecules ranging in size from 5 to 400 nm were observed in the spines of different sea urchin species (*Anthocidaris crassispina*, *Holopneustes porossimus*, and *Heterocentrotus trigonarius*).[37,49,50]

By previously applying the heat-stimulated crystallization of remnant ACC and destruction of intracrystalline organic molecules in sea urchin skeletal elements, we observed the evolution of calcite lattice distortions due to strong atomic interactions at the organic−inorganic interfaces.[38] Here, we focus on the evolution of pores at different length scales, which compensate the mineral volume shrinkage during ACC crystallization and organics removal in these biominerals. For this purpose, we use *in situ* heating synchrotron small-angle X-ray scattering (SAXS) for the quantification of nanometer-sized (from 2 to 100 nm) pores, scanning electron microscopy (SEM) and focused ion beam (FIB)-SEM serial imaging techniques for the visualization of 3D nanometer- and micrometer-sized (from 100 nm to 5 μm) pores, and SEM and microcomputed X-ray tomography (CT) for the characterization of macrometer-sized (from 5 to 25 μm) pores.

2. EXPERIMENTAL SECTION

2.1. Materials and Sample Preparation. Sea urchin specimens of *P. lividus*, collected in the Atlantic Ocean, were received from the Roscoff biological station of Sorbonne University (France). They were first dissected to remove the Aristotle's lantern (echinoid mouthparts), the coelomic fluid, and the internal organs.[51] Second, they were soaked in 200 mL of 5% sodium hypochlorite (NaClO) solution for 3 h, allowing for the spines to detach from the test by destroying most of the organic tissues (podia, muscles, epidermis, etc.). The spines and the tests were rinsed with distilled water and air-dried. Spines and individual interambulacral test plates were then suspended again in a 5% NaClO solution for 5 h under agitation to remove the remaining external organic material, i.e., the intercrystalline organic molecules. They were finally rinsed five times with distilled water and air-dried.

Fifteen spines were annealed at fixed temperatures ranging from 100 to 400 °C in a Nabertherm 30−3000 °C oven equipped with a controller P320. For *ex situ* heating SAXS measurements, the preannealed spines were embedded in epoxy resin and cut with a diamond saw under water to obtain ∼250 μm sections having different orientations (90 and 45°) with respect to the calcite *c*-axis of the spine. For *in situ* heating SAXS experiments, 5 interambulacral test plates and 10 spines were measured. For SEM observations, in total 40 spines and test plates were preannealed at different temperatures with a temperature ramp of 2 °C/min in a Linkam heating stage used for SAXS experiments (see below) and then cooled down at room temperature before observation. They were then fractured, carbon coated, and examined. Finally, for FIB-SEM measurements, two spines were preannealed, respectively, at 350 and 450 °C for 1 h and one interambulacral test plate at 450 °C for 1 h and then embedded in epoxy resin, cut, and polished.

2.2. Synchrotron SAXS Measurements. SAXS measurements were performed at the μSpot beamline of the BESSY II synchrotron radiation facility (HZB, Helmholtz-Zentrum Berlin für Materialien und Energie, Berlin, Germany), using an X-ray spot size of 100 μm and a multilayered (MoBC) monochromator (wavelength of 0.82656 Å).

The two-dimensional scattering patterns were recorded using a MAR-detector (MARCCD 225, MAR USA, Evanston, USA) having (3072 × 3072) px^2 and (73.24 μm)^2 pixel size. The sample−detector distance was 82 to 83 cm. Measurement times varied from 1 to 5 s. A silver behenate powder standard was used for calibration. In addition, the background due to air scattering and the closing window of the Linkam FTIR600 (see below), as well as the X-ray transmission through the samples, were measured for data analysis. X-ray transmission was measured at room temperature before *in situ* heating and during heating as its intensity slightly varies with temperature.

For *in situ* heating SAXS experiments, samples were glued at their extremities on aluminum frames with an Epoxy-Kleber glue (Gluetec) (Figure SI1A,B) and mounted on a Linkam (Linkam FTIR600, Linkam Scientific Instruments, Surrey, UK). Temperature ramps of 2 and 3 °C/min were applied. The test plates were oriented with the calcite *c*-axis perpendicular to or aligned with the X-ray beam. However, due to the elongated shape of the spines, with their *c*-axis aligned with it, it was only possible to orient them with the *c*-axis perpendicular to the beam. Therefore, in order to also measure the spines with their *c*-axis aligned with the beam, transverse sections (cut at 90° to the *c*-axis) were obtained (see 2.1.).

2.3. SAXS Data Analysis. Azimuthal integrations of the 2D scattering patterns were performed using the software Fit2D (A. Hammersley, ESRF, Grenoble, France). In this way, the averaged scattering intensities, $I(q)$, were obtained, as a function of the scattering vector $q = 4\pi \sin(\theta)/\lambda$, with 2θ being the scattering angle. Background and transmission corrections were applied. At room temperature, the corrected SAXS intensity profiles show a shoulder around 1.5 nm^{-1} (see 3.3.). This shoulder shifts to lower q at higher temperatures, indicating an increase in the average size of the scattering objects. This shift is better revealed in the Kratky plots,[52] $[I(q) - B]q^2$ vs q, where B is the

https://doi.org/10.1021/acs.cgd.2c00083
Cryst. Growth Des. 2022, 22, 3727−3739

Laue constant, which is determined by calculating the averaged SAXS intensity in the q range between 7 and 10 nm^{-1} (Figure SI2). For a few temperatures, the obtained Laue constants were verified by constructing the Porod plot, $[I(q)q^4]$ vs q.[52] To quantify the increase in size of the scattering objects, the SAXS data were analyzed to extract the radius of gyration (R_g) and the Porod length (T_p parameter).[52,53] These parameters differ in averaging procedures, providing the characteristic size of the scattering objects. For example, for spherical particles with different radii, R, and for point collimation of incoming X-rays, the radius of gyration is:[54]

$$R_g = \sqrt{\frac{3}{5}\frac{\langle R^8\rangle}{\langle R^6\rangle}} \quad (1)$$

In turn, the Porod length is defined by the ratio of the average pore volume to the average surface area, and in the case of a small volume fraction of spherical pores it is:[53]

$$T_p = \frac{4}{3}\frac{\langle R^3\rangle}{\langle R^2\rangle} \quad (2)$$

T_p parameter analysis was done using the software DPDAK[55] applied to Porod plots[52,53] (Figure SI3A,B).

For the R_g analysis, the SAXS intensity profiles were fitted with a contribution from a Porod function and from a Guinier−Porod function[56] (Figure SI3C):

$$I(q) = I_0 + I_{p_1}q^{-d_1} + I_g e^{-1/3q^2R_g^2}, \text{ for } q < q_1$$

$$I(q) = I_0 + I_{p_1}q^{-d_1} + I_{p_2}q^{-d_2}, \text{ for } q > q_1$$

$$\text{with } I_{p_2} = I_g e^{-d_2/2}\left(\frac{3}{2}d_2\right)^{d_2/2} R_g^{-d_2} \text{ and } q_1 = \frac{1}{R_g}\left(\frac{3}{2}d_2\right)^{1/2}$$

where, d_1 and d_2 are the Porod exponents for the two Porod contributions, while I_{p1}, I_{p2}, and I_g are the Porod and Guinier scale factors. This expression allows extracting R_g as a function of temperature.

Finally, the total integrated scattering intensity was calculated, as $I_{tot} = \sum \{[I(q) - B]q^2\}$, to uncover potential changes in the total pore volume as a function of temperature.

2.3.1. Streak Analysis. The [100]-like streaks of diffuse scattering, appearing from 300 °C upward, were analyzed to evaluate the size and the angular spread of the scattering objects responsible for such streaks.[57] First, the SAXS signals of the spines were rotated by 2° and those from the test plates by 18° aimed at setting the streaks vertically (Figure SI4A). A coordinate system was defined with q_y perpendicular to the streak and q_z aligned with the streak (Figure SI4A). Second, a custom-made Python script allowed extracting the scattering intensity $I_{meas}(q_y)$ across several slices being perpendicular to the streaks and therefore having different q_z values (as an example see Figure SI5A for $I_{meas}(q_y)$ at $q_z = 0.583$ nm^{-1} for the spine and test plate samples annealed at 450 °C). Third, the $I_{meas}(q_y)$ profiles were fitted with a Gaussian function, $y_0 + \frac{A}{\sigma\sqrt{2\pi}}e^{-(x-x_0)^2/\sigma^2}$, in order to define the cropping boundaries of the data, and then with another Gaussian function, $I_{meas}(q_y) = y_1 + b\cdot e^{-1/4\cdot q_y^2\cdot R_{fit(q_z)}^2}$, where $R_{fit(q_z)} = \frac{\sqrt{4\cdot\ln 2}}{k_{meas(q_z)}}$ is the two-dimensional radius of gyration and $k_{meas(q_z)}$ is the half-width at half-maximum (HWHM) of the scattering intensity $I_{meas}(q_y)$ across the streak at a specific q_z.[57] As examples, see Figure SI5B and SI5C showing, respectively, the $I_{meas}(q_y)$ profiles taken at $q_z = 0.583$ nm^{-1} from the spine and test plate samples at 450 °C. In addition, $R^2 = \frac{4\cdot\ln 2}{k_0^2 - k_{res}^2}$, with $k_0 = k_{meas}(q_z = 0)$, which can be determined by plotting and linearly fitting ${k_{meas}}^2$ vs ${q_z}^2$. Here, ${k_{meas}}^2({q_z}^2) = k^2 + {k_{res}}^2 + {k_\alpha}^2{q_z}^2$, where k_{res} is the HWHM of the resolution function, the parameter, k, is the corrected HWHM, and k_α is the angular spread.[57] Thus, $k_{meas}(q_z = 0)$, i.e., $\sqrt{k^2 + k_{res}^2}$, and k_α are obtained as a function of temperature (Figure SI5D−F), and the sizes of the scattering objects, R, can be estimated.

2.4. Laboratory SAXS Measurements. Laboratory SAXS measurements were performed with a Bruker Nanostar equipment and a Cu X-ray source (wavelength 1.5418 Å for Cu Kα). 2D SAXS signals were recorded with a 2D Vantec-2000 detector ((2048 × 2048) px^2, (68 μm)^2 pixel size) (Figure SI1C). The beam size was 115 μm, the sample−detector distance was 111 cm, the q-probe region was 0.04 to 3.25 nm^{-1}, and the measurement time was 6 h.

2.5. SEM and FIB/SEM Observations. SEM observations and FIB/SEM serial imaging were performed, respectively, with a Gemini 1550 and a Crossbeam 540, Zeiss microscopes.

For FIB/SEM serial imaging, volumes from 100 to 340 μm^3 were FIB-sliced and SEM-viewed in the galleried stereom (thin trabeculae) of the test plates annealed at 450 °C and in the septa of the spines annealed at 350 and 450 °C. The voxel volumes were $(18.34\ nm)^3$ and $(9.3\ nm)^3$ for the samples annealed at 350 and 450 °C, respectively. The SEM image stacks were corrected (destriped and aligned) using custom-made Python scripts. After correction, the pores were segmented using a deep learning approach with a simple U-Net.[58] The pores were further analyzed with a 3D analysis counter and viewed with a 3D viewer tool FIJI. Finally, 3D Fourier transforms were applied to the FIB/SEM volumes after thresholding and integrated with a custom-made Python script (Figure SI9).

2.6. Computed Tomography. CT experiments were performed at the Tomcat beamline of Swiss Light Source Synchrotron. Three volumes, (1.7 × 1.7 × 1.4) mm^3 each, were probed at the tip, the base, and in the middle of a spine. A 10× objective was used, which implies a voxel size of $(0.65\ \mu m)^3$. 3D volume rendering and segmentation allowing the quantification of macroporosity were performed automatically with Amira 3D (FEI) software.

3. RESULTS AND DISCUSSION

3.1. Macroporosity of *P. lividus* Sea Urchin Test Plates and Spines. The endoskeleton of sea urchins, the test, is composed of individual plates, which are assembled in a five-point radial symmetry.[16] Each individual plate diffracts X-rays as a single crystal of calcite, with its c-axis tangent to the surface of the test in the case of the *P. lividus* species.[16] On the outer surface of the interambulacral plates (Figure 1A, dashed curved lines), numerous protuberant tubercles of different sizes (0.1 to 2 mm) are observed; they are the attachment sites of the spines and are polycrystalline.[16]

By studying the interambulacral plates of about 30 different sea urchin species, 10 distinct types of stereom have been described and classified, which vary in terms of geometry and dimensions of the struts and pores.[59] In *P. lividus*, the labyrinthic, galleried, and perforate stereoms were identified.[59] They, respectively, consist of a disorganized mesh of trabeculae, an organized mesh of long parallel galleries running in a certain direction, and a mesh of trabeculae thicker than the pore diameters. These three types of stereom spatially vary throughout the plate as shown by the SEM micrographs in Figure 1B−F. The labyrinthic stereom is observed on the outer surface (Figure 1C,B) as well as within the plate (Figures 1D,E and SI6A) below the main tubercle. The galleried stereom is located within the plate only (Figures 1D,F and SI7A), while the perforate stereom is present both at the inner surface (Figure 1D,E) and within the plate (Figure SI6A). The pore and strut diameters in the different types of stereom are documented in Table SI1. The labyrinthic and galleried stereom present slender struts (8 to 12 μm in diameter) and are named hereafter "thin" trabeculae, whereas the perforate stereom composed of thick struts (20 to 30 μm in diameter) is referred to as "thick" trabeculae.

The test of sea urchins is surrounded by sacrificial appendages, the spines that also diffract X-rays as single crystals of calcite and have the calcite c-axis aligned with their long axes. In this study,

https://doi.org/10.1021/acs.cgd.2c00083
Cryst. Growth Des. 2022, 22, 3727−3739

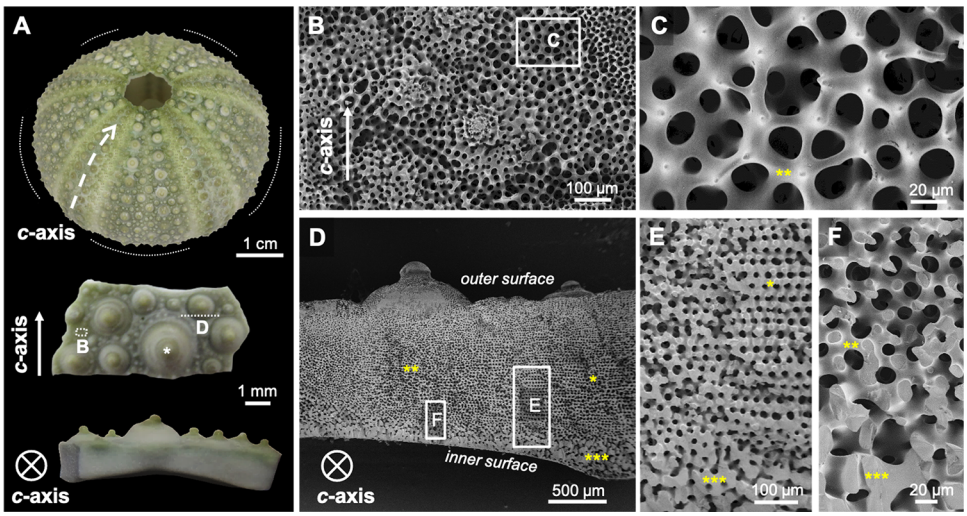

Figure 1. Morphology of *P. lividus* interambulacral test plates whose organic tissues were removed by NaClO treatment. (A) Top: test of a sea urchin with the interambulacral plates indicated by dashed curved lines, bottom: interambulacral plate with its *c*-axis parallel or perpendicular to the surface (*tubercle) (photograph G. Laurent, Sorbonne Université); SEM micrographs of (B) outer surface of the plate indicated in bottom (A), showing the labyrinthic stereom; (C) magnification of the labyrinthic stereom of (B) and (D) fractured section perpendicular to the *c*-axis indicated in bottom (A), showing the galleried stereom (marked by yellow *), labyrinthic stereom (marked by yellow **), and perforated stereom (marked by yellow ***); and (E, F) magnification indicated in (D). The orientation of the calcite *c*-axis is indicated by a white arrow or a crossed-circle.

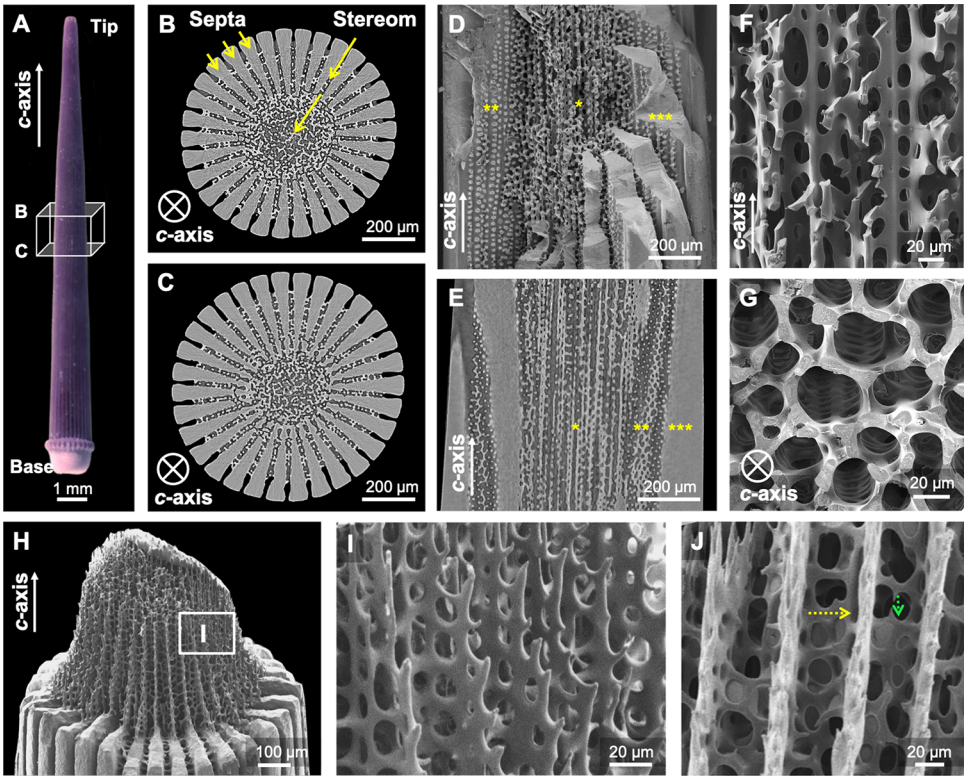

Figure 2. Morphology of *P. lividus* sea urchin spines whose organic tissues were removed by NaClO treatment. (A) Fully developed spine, specific volumes for further CT investigation are marked by letters B and C; (B and C) CT images of virtual sections perpendicular to the *c*-axis and, respectively, located closer to the tip and the base as indicated in (A), the septa and the two types of stereom (labyrinthic and laminar) are shown; (D) SEM micrograph of a fractured spine close to the base; (E) CT image of a virtual section along the *c*-axis; (F and G) SEM micrographs of the laminar inner stereom taken, respectively, with sections along and perpendicular to the long axis of the spine; (H and I) growing spine showing the laminar stereom arranged in radial sheets aligned with the septa; and (J) laminar radial sheets connect through horizontal struts (yellow arrow) that split vertically (green arrow), the laminar stereom is indicated by *, labyrinthic stereom by **, and septa by ***. The orientation of the calcite *c*-axis is indicated by white arrow or a crossed-circle.

we investigate the spines, which are about 1 to 1.5 cm long (Figure 2A). The main difference in terms of stereom macrostructure between the spines and the test plates is the presence of imperforate stereom in the spines. The imperforate stereom is described as "a solid layer of calcite with no pores";[59] in other words, it is a continuous volume mainly composed of

https://doi.org/10.1021/acs.cgd.2c00083
Cryst. Growth Des. 2022, 22, 3727−3739

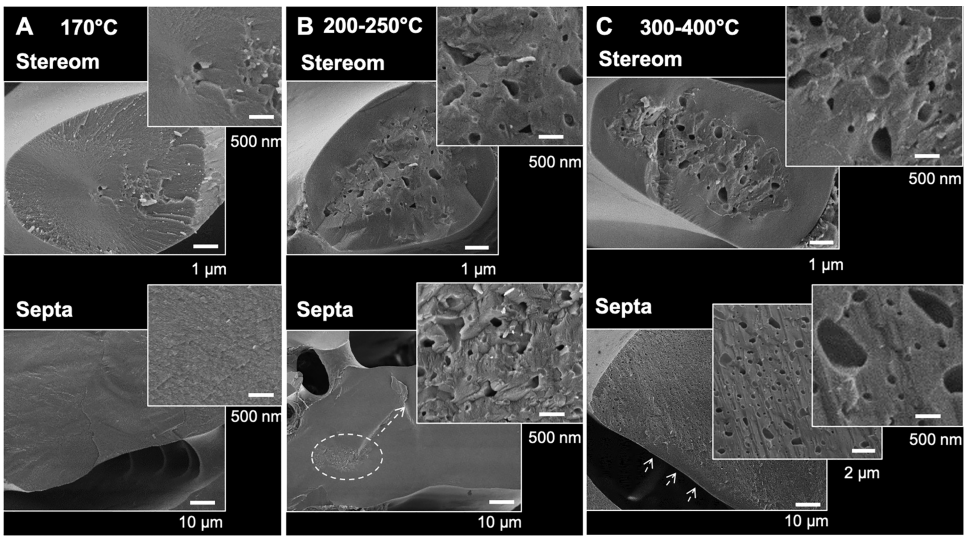

Figure 3. SEM micrographs of the laminar stereom and the septa regions of fractured sections in the middle of the spines annealed at: (A) 170 °C; (B) between 200 and 250 °C; and (C) between 300 and 400 °C. Dashed arrows show the outer layer with no observable pores.

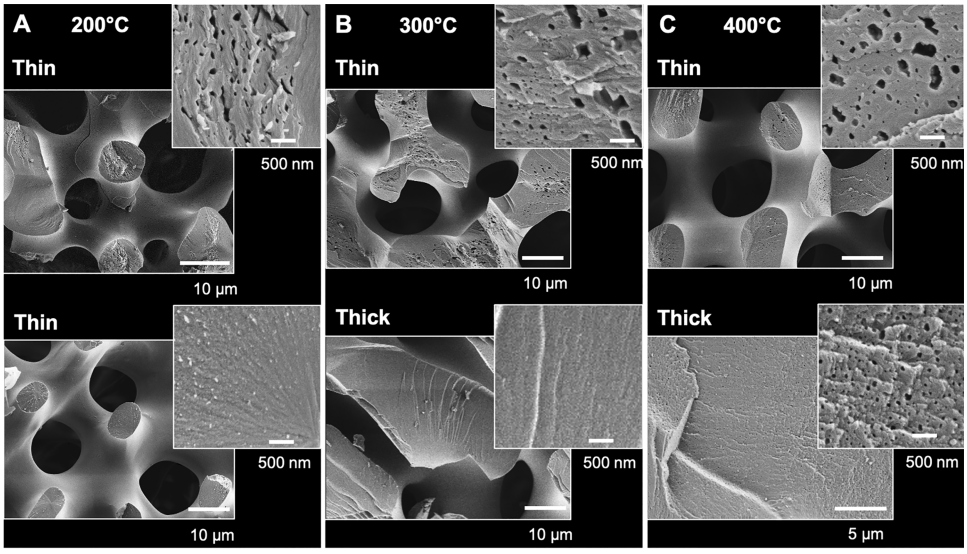

Figure 4. SEM micrographs of the thin (labyrinthic or galleried) and thick (perforate) trabeculae of the stereom of fractured test plates annealed at: (A) 200 °C; (B) 300 °C; and (C) 400 °C.

calcite. It constitutes the outer wedges of the *P. lividus* spines, the septa, which are arranged radially around the center of the spines (Figure 2). According to Smith's terminology,[59] the center of the *P. lividus* spines is composed of a laminar stereom whose lamellar sheets are radially oriented (Figure 2H,I). The lamellar sheets are connected to each other through numerous perpendicular struts that often split vertically (Figure 2J) leading to a dense meshwork, which looks like a galleried stereom when viewed on transverse sections (Figure 2G). The struts of the laminar stereom are thinner than the "thin" trabeculae of the test plates (Table SI1). Finally, a labyrinthic stereom is also present in between the septa of the spines, with struts and pores of similar diameters (Figure 2B–E and Table SI1).

Computed tomography measurements performed at the tip, the middle, and close to the base of one spine show that the volume fraction of the septa and the macroporous stereom varies along the spine. Virtual CT sections perpendicular to the long axis of the spine reveal that close to the base, the septa become longer and wider, while the total diameter of the inner stereom is smaller than that close to the tip (Figures 2B,C and SI7). The segmentation of the CT volume measured in the middle of the spine allowed quantifying the total volume fraction of the septa (57 vol %), the stereom (9 vol %), and the macropores (34 vol %).

3.2. Micropore Formation during ACC Crystallization and Organic Degradation. *3.2.1. SEM Observations.* The presence of internal interfaces in biominerals formed after heat treatments were previously identified[24] and micropores were reported in sea urchin spines annealed at 450 °C.[37] Therefore, to visualize the presence of micropores in the heat-treated samples, we performed SEM observations on fractured surfaces, previously annealed at temperatures characteristic for ACC crystallization and organic molecule degradation[38] (Figures 3 and 4). According to previously reported[38] thermogravimetric analysis (TGA) coupled either with differential scanning calorimetry (DSC) or mass spectrometry (MS) measurements, the crystallization of remnant ACC ($Ca{:}0.1H_20$) associated with

https://doi.org/10.1021/acs.cgd.2c00083
Cryst. Growth Des. 2022, 22, 3727−3739

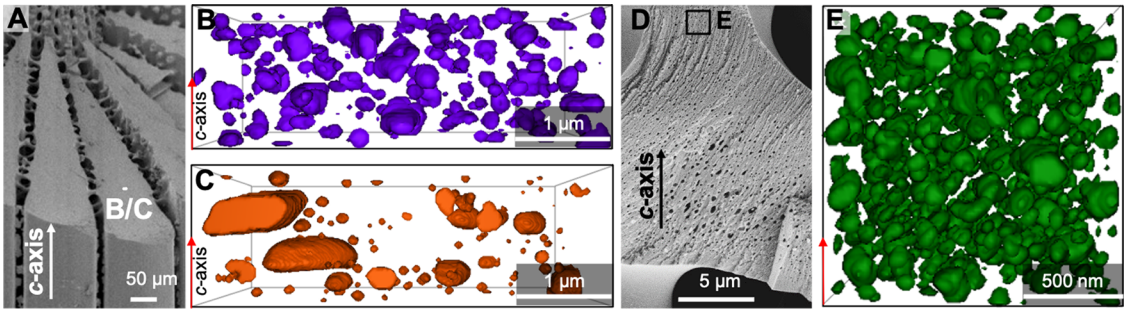

Figure 5. Microporosity revealed by SEM and FIB-SEM. (A) SEM micrograph of the septa of a fractured spine; the location of the volumes milled for FIB-SEM in the septa is marked by letters B and C; FIB-SEM 3D visualization of the pores of a septum of a spine annealed for 1 h at: (B) 350 °C and (C) 450 °C; (D) SEM micrograph of the thin trabeculae of a fractured test plate annealed at 450 °C; the location of the volume milled for FIB-SEM is marked by letter E; and (E) FIB-SEM 3D visualization of the pores of the thin trabeculae of a test plate annealed for 1 h at 450 °C. The orientation of the *c*-axis is indicated by a red arrow.

water loss is maximal around 200 °C for both the spines and the test plates, whereas organic destruction is maximal around 270 °C for the spines and 370 °C for the test plates. Under these conditions, the characteristic sizes and spatial distributions of pores with diameters larger than 20 nm (detection limit estimated for the fractured sections) have been investigated in the septa and the laminar stereom in the center of several spines and in the galleried and perforate stereom of several test plates.

The spines were fractured roughly perpendicular to their *c*-axes around the middle of the shaft length. The first pores detectable by SEM are observed in samples heated at 170 °C (Figure 3A). At this temperature, ACC crystallization begins[38] and likely initiates pore formation due to significant volume change and mass transport within the biomineral. In addition, water release due to ACC crystallization and possibly due to organic dehydration may also contribute to pore evolution at this temperature. Indeed, water present in the pristine samples was shown to strongly bond to carbonates from ACC;[38] however, some water could also be associated with organics, especially taking into account the close interrelation of ACC and organics in these biominerals.[38] The pores having diameters from 20 to 100 nm are located in the center of the struts of the inner laminar stereom. Small pores are spherical, while large ones occasionally exhibit faceted edges (cubelike). ACC crystallization in localized areas may lead to the formation of pores developing shapes that geometrically resemble the equilibrium crystal shape of calcite,[60] suggesting the crystallization of the new mineral to be coherent with the pre-existing calcite.

Between 200 and 250 °C, when ACC crystallization rate is maximal, the number of observable pores increases in the struts of the inner laminar stereom: ∼50 nm pores are spherical in shape, ∼250 nm pores are faceted (cube- and triangle-like shapes), while ∼450 nm pores present convoluted shapes (Figure 3B, laminar stereom). The pores are located preferentially in the middle of the struts, whereas an external circumferential layer, ∼1.3 μm wide, with no detectable pores is also present. At these temperatures, some pores also appear in the septa, but in limited areas. Some 30 to 80 nm round pores are observed, as well as few 100 to 250 nm faceted pores (Figure 3B, septa).

Between 300 and 400 °C, when ACC crystallization is complete and organic molecule degradation is maximal, the size and the number of pores increase slightly in the inner stereom and more significantly in the septa (Figure 3C). In the septa, small pores of 50 to 100 nm are observed together with elongated micropores (up to 1.3 μm long). In some fractured sections, pores cover the whole septum area (Figure SI8). However, in most cases, a 7 to 10 μm wide outer region along the septum length without detectable pores is visible (Figure 3C in the septa panel and Figure SI8).

In the case of the test plates, where ACC crystallization also occurs between 170 and 250 °C, pores start to be detected at 200 °C. They are only observed in some fractured struts of the thin trabeculae of the stereom and are mainly located in the middle of the struts (Figure 4A). Similarly to the spines, a circumferential outer layer with no detectable pores is present in the test plates. The 20 to 100 nm round pores and 100−300 nm elongated or asymmetrical pores are observed together with few faceted pores.

At 300 °C, pores are detected in all the examined thin trabeculae of the stereom. More pores are visible in the middle of the struts, the 150 to 650 nm pores are faceted (cubelike shape) and the 30−100 nm ones are rounded (Figure 4B). Nevertheless, a 3 to 4 μm wide pore-free zone persists, and the thick trabeculae does not show detectable pores. At 400 °C, the size and the spatial distributions of the pores remain the same in the thin trabeculae, whereas the pores are increasing in size in the thick trabeculae (Figure 4C). In the latter, the 20 to 150 nm rounded pores are homogenously distributed within the struts.

In summary, upon heating, micropores are observed with heterogeneous spatial distributions in both samples and with different temperature-dependent appearances. The micropores form at the lowest temperature in the laminar stereom (170 °C) of the spines, then in the thin trabeculae of the test plates and in the septa of the spines (200 to 250 °C). At higher temperatures, they are present all over the septa (300 to 400 °C), and only above 400 °C, they appear in the thick stereom of the test plates. Interestingly, the sequence of pore appearance with increasing temperature correlates with the reported growth rates of the different macromorphologies, i.e., ∼100 μm/day in length for the laminar stereom of the spines, ∼20 μm/day for the thin trabeculae of the test plates, ∼10 μm/day for the septa, and 4 μm/day for the thick trabeculae of the test plates.[61]

3.2.2. FIB-SEM Serial Imaging. FIB/SEM measurements were performed at 350 and 450 °C for the spines and at 450 °C for a test plate in order to investigate further the total volume of micropores (with diameters >10 nm), their density, shape, and orientation in 3D once formed after organics destruction (Figures 5 and SI9 and Table SI2). The FIB/SEM volumes (100−340 μm^3) were measured in a septum of the annealed

https://doi.org/10.1021/acs.cgd.2c00083
Cryst. Growth Des. 2022, 22, 3727−3739

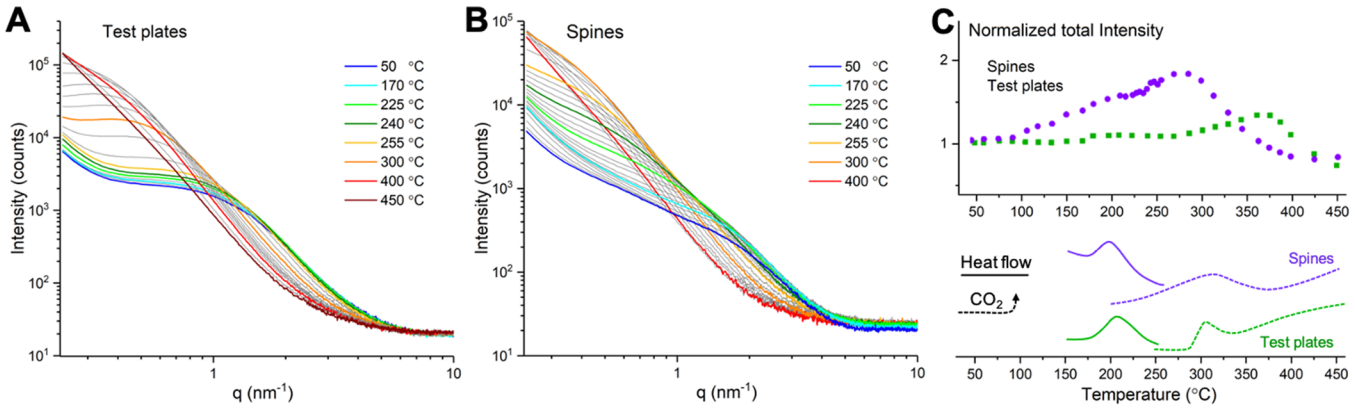

Figure 6. SAXS intensity profiles for selected temperatures as a function of scattering vector q, in a loglog scale for: (A) test plates and (B) spines. (C) Normalized total scattering intensity (to pristine state) for the spines and the test plates as a function of temperature. The temperature ranges for ACC crystallization (heat flow, DSC data, and plain lines) and organics destruction (CO_2 emission, TGA-MS data, dashed lines) from ref 38 are indicated in purple for the spines and in green for the test plates.

spines and in a thin trabecula in the galleried stereom of an annealed interambulacral test plate.

The results show that organics degradation in the septum of the spines leads to the formation of larger pores (up to 2.6 μm) at 450 °C than at 350 °C. The small pores appear spherical, whereas the large ones have clear ellipsoidal shapes. Taking these shape variations into account, we conclude that the pore size varies between 20 nm and 1 μm in the spine annealed at 350 °C and between 30 nm and 2.6 μm in the spine annealed at 450 °C. The largest elongated pores are clearly oriented with their long axis perpendicular to the spine c-axis (Figure 5B,C). Different pore densities of 40 and 10 μm^{-3} were found in the spines annealed at 350 and 450 °C, with however, similar total pore volumes of 4 and 5.5 vol %, respectively (Figure SI9D). This might suggest an Ostwald ripening type coarsening mechanism.[62]

At 450 °C, the thin trabeculae of the test plate show smaller and more spherical pores than the septum of the spine, with diameters ranging from 10 to 350 nm (Figure 5E). The pore density is also higher in the test plate (285 μm^{-3}) than that in the spine (10 μm^{-3}) but similar total pore volumes (8.3 vol % vs 5.5 vol %) were measured in agreement with similar amounts of ACC (about 10 wt %) and intracrystalline organics (about 1.6 wt %) present in both samples.[38] We suggest that these variations in the microstructure after annealing might be due to the different inorganic−organic interactions present in both samples. Indeed, we previously showed that organics preferentially attached to the crystallographic planes parallel to the c-axis of calcite in the spines, while they equally attached to the planes parallel and perpendicular to the c-axis in the test plates.[38]

Finally, 3D fast Fourier transform (FTT) analysis was applied to the FIB/SEM volumes in order to determine the orientation of the pores. The azimuthally integrated profiles report the intensity of the FFT as a function of the reciprocal space vector q (nm^{-1}) (Figure SI9). The profiles show a shoulder around 0.03 nm^{-1} for the spine at 350 °C and the test plate at 450 °C, which is related to the real-space dimensions of the observed microporosity. For the spine annealed at 450 °C, the shoulder shifts to lower q (0.003 nm^{-1}) indicating that on average, the micropores indeed increase in size from 350 to 450 °C.

3.3. Nanopore Formation during ACC Crystallization.

In situ heating SAXS experiments were performed to extend the analysis of the nano- and micro-pore evolution into early stages where pore size is smaller than 100 nm. The samples were mounted with their c-axes perpendicular to the X-ray beam, and the SAXS measurements were performed in between the tubercles of the test plates and in the middle of the spines. Therefore, the macrostructures probed were mainly the thin trabeculae of the test plates and the dense septa of the spines. Figure 6A,B displays the temperature-dependent SAXS profiles, $I(q)$, obtained after azimuthal integration of the scattered intensity of the 2D SAXS patterns presented in Figure SI1A,B and recorded during in situ heating of the test plates and spines. In addition, Figure 6C shows the total integrated SAXS intensities (over q and normalized to those in pristine samples), as a function of temperature for both samples, where the total integrated SAXS intensity is proportional to the total pore volume.[52] The obtained data allow extracting quantitative information on the nanopore evolution as follows.

The SAXS profiles of the samples annealed at 50 °C show a shoulder at ~1.5 nm^{-1} for the test plates and at ~2 nm^{-1} for the spines, originating in nanodomains (or nanopores) with electron densities differing from that of the mineral. Pristine samples contain anhydrous ACC[38] for which the electron density is comparable to that of calcite[27] and cannot significantly influence the SAXS signals. Therefore, we suggest that at the pristine stage, the nanopores are filled with hydrated organics rather than ACC as previously proposed.[37]

Upon heating, the shoulder shifts to lower q values for both samples, manifesting an increase in size of the nanopores. This shift is clearly seen in the Kratky plots, $[I(q) - Bq^2]$, with B being the Laue constant (Figure SI2). The SAXS profiles can be subdivided into three regions (I, II, and III) according to the position of the shoulder: (I) the low q region, $q < 0.3$ nm^{-1}, which shows linear intensity decay with q; (II) the intermediate region, $0.3 < q < 1.5$ or 2 nm^{-1}, presenting a plateau; and (III) the high q region, $q > 1.5$ or 2 nm^{-1}, with intensity asymptotically approaching to zero. Upon heating, all three regions are shifted to lower q values. Above certain temperatures, T_m, regions (I) and (II) gradually disappear from the probed q range window, indicating that at these temperatures the averaged nanopore size becomes larger than 100 nm (the maximum size of the scattering objects measurable at the μSpot beamline[63]). These pores are likely the micropores seen in the SEM and FIB/SEM observations for which the shoulder of the integrated Fourier transforms is at 0.03 nm^{-1} (Figure SI9). Thus, the reciprocal space (q range) probed by the SAXS set up (0.3 to 10 nm^{-1}) is

https://doi.org/10.1021/acs.cgd.2c00083
Cryst. Growth Des. 2022, 22, 3727−3739

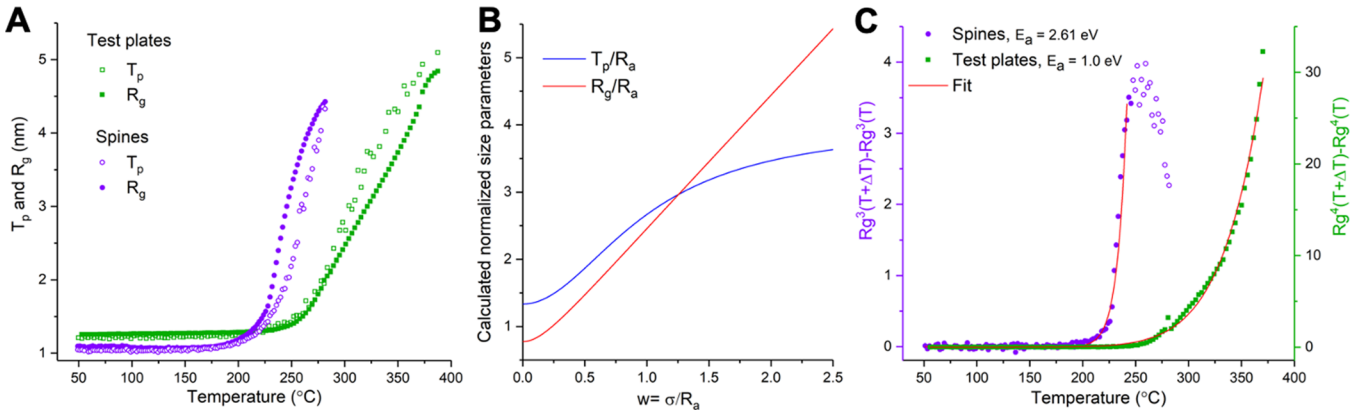

Figure 7. Increase in the nanoporosity as a function of temperature. (A) Temperature-dependent magnitudes of the R_g and T_p parameters extracted from SAXS data for the test plates and the spines up to T_m; (B) normalized size parameters, T_p/R_a and R_g/R_a, calculated by eqs 4 and 5, as a function of the reduced distribution width, $w = \sigma/R_a$; and (C) best fits of temperature-dependent increments, $R_g^n(T + \Delta T) - R_g^n(T)$, to eq 8 for the spines (in purple) and the test plates (in green), providing, respectively, $n = 3$, $E_a = 2.61$ eV and $n = 4$, $E_a = 1.0$ eV.

extended to smaller q (i.e., larger real-space dimensions) with the aid of FIB-SEM data.

The characteristic nanopore size was extracted from the SAXS data by calculating the T_p parameter and radius of gyration, R_g, up to T_m (see the Section 2 and Figure SI3A–C). For the spines, T_m = 270 °C and for the test plates, T_m = 370 °C, which correspond to the maximum weight loss due to organics destruction in both samples, respectively.[38]

Before annealing, the nanopores in the test plates and spines are characterized by similar T_p and R_g values equal to 1.23 and 1.05 nm, respectively (Figure 7A). With increasing temperature, the nanopores become larger with the most substantial growth observed above 250 °C for the test plates and 200 °C for the spines, correlating with ACC crystallization temperatures.[38]

We stress that above ∼280 °C for the test plates and ∼230 °C for the spines, the measured R_g and T_p parameters behave differently: $R_g < T_p$ in the test plates and $R_g > T_p$ in the spines (Figure 7A). We relate these differences to the temperature-mediated variations in the width of the statistical distributions of the nanopore size. This statement can be illustrated using Gaussian distribution of spherical nanopores characterized by radius, R:

$$G(R) = \frac{1}{\sigma\sqrt{2\pi}}\exp\left[-\frac{(R - R_a)^2}{2\sigma^2}\right] = \frac{1}{\sigma\sqrt{2\pi}}\exp\left(-\frac{x^2}{2\sigma^2}\right) \quad (3)$$

where R_a is the radius mean value, $x = R - R_a$, and σ is the standard deviation, which defines the width of the Gaussian distribution. Considering eqs 123, one can calculate the radius of gyration, R_g:

$$R_g = \sqrt{\frac{3}{5}\frac{\langle R^8\rangle}{\langle R^6\rangle}} = R_a\sqrt{\frac{3}{5}}\sqrt{\frac{1 + 28w^2 + 210w^4 + 420w^6 + 105w^8}{1 + 15w^2 + 45w^4 + 15w^6}} \quad (4)$$

and the Porod length, T_p:

$$T_p = \frac{4}{3}\frac{\langle R^3\rangle}{\langle R^2\rangle} = \frac{4}{3}R_a\frac{1 + 3w^2}{1 + w^2} \quad (5)$$

as a function of the width of distribution and parameter, R_a, via the ratio, $w = \frac{\sigma}{R_a}$. The w-dependences of the normalized parameters, R_g/R_a and T_p/R_a, are plotted as shown in Figure 7B. For w = 1.25, $R_g/R_a = T_p/R_a$ (as observed in pristine samples), for $w < 1.25$, $R_g/R_a < T_p/R_a$ (as observed in the test plates above ∼280 °C), and for $w > 1.25$, $R_g/R_a > T_p/R_a$ (as observed in the spines above ∼230 °C). We therefore suggest that at the temperatures mentioned the nanopore size distribution becomes narrower ($w < 1.25$) in the test plates whereas broader ($w > 1.25$) in the spines. Note that this temperature interval corresponds to the end of ACC crystallization and the beginning of organic decomposition.[38]

Most interesting finding, however, is the growth of the nanopore size upon heating (Figure 7A), which manifests the classical phenomenon of Ostwald ripening via pore coarsening. The coarsening allows the reduction of the system's free energy because the surface to volume energy contribution scales as $R^2/R^3 \propto 1/R$. For classical Ostwald ripening, the total nanopore volume remains constant during the coarsening process, i.e., larger pores grow at the expense of smaller ones. The total nanopore volume evolution upon *in situ* heating of the spines and test plates can be appreciated by considering the total integrated SAXS intensities (Figure 6C). The total SAXS intensities and therefore the total nanopore volumes are nearly constant up to T_m for both samples. Nevertheless, some increase is observed mainly in the spines (up to 1.8 at 270 °C), suggesting the formation of new nanopores in addition to the coarsening mechanism. Thus, the nanopore evolution occurs mainly via coarsening in the macroporous test plates, whereas additional nanopores are formed in the dense spines. After T_m, the total SAXS intensities decrease for both samples since nanopores that become larger than 100 nm are no longer detectable in the probed q range window.

In order to further characterize the coarsening mechanism in both samples and extract the activation energies, E_a, of the respective diffusion processes, the following procedure was applied. Thermodynamic theories of Ostwald ripening[62] predict the growth with time, t, of the average pore radius, R_a, at constant temperature from a starting value $R_a(0)$ at $t = 0$, as:

$$R_a^n = R_a^n(0) + Kt \quad (6)$$

where K is some temperature-dependent parameter,[60] which is proportional to:

https://doi.org/10.1021/acs.cgd.2c00083
Cryst. Growth Des. 2022, 22, 3727−3739

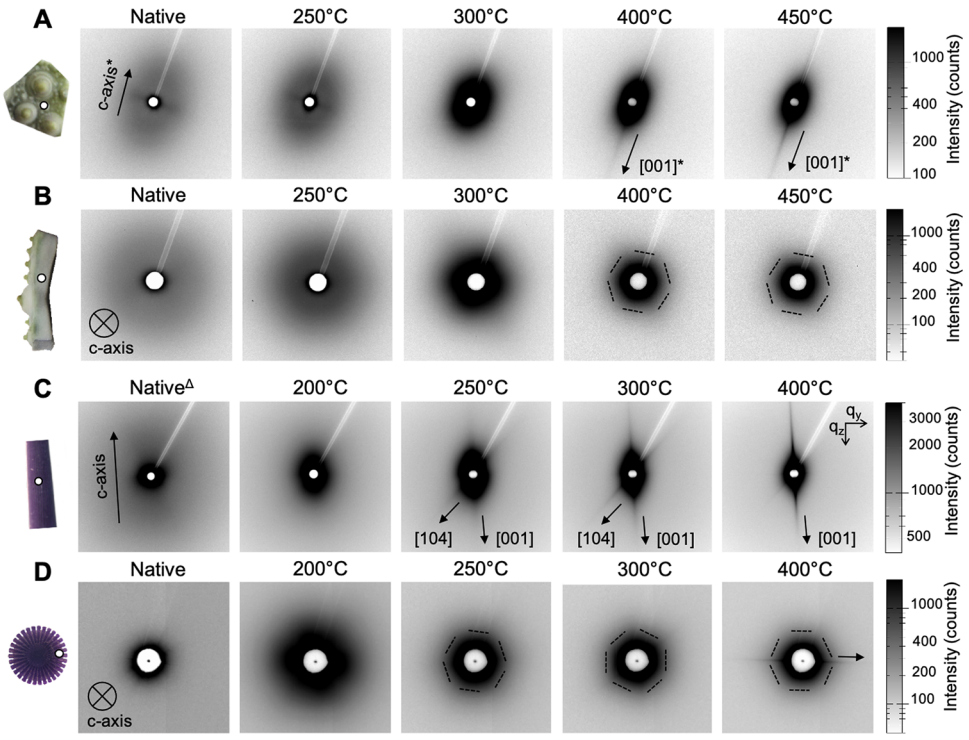

Figure 8. 2D SAXS patterns of native and annealed samples. (A) Test plate oriented with its *c*-axis perpendicular to the beam, *orientation of the *c*-axis and thus the [001] direction obtained with laboratory SAXS measurements (Figure SI1C); (B) test plate with its *c*-axis aligned with the beam; (C) spine oriented with its *c*-axis perpendicular to the beam, ^Δthe scale of the intensity for this SAXS pattern is from 400 to 2000 counts (in Figure SI1D different scales are reported); and (D) transverse sections of different spines. The samples in (A−C) were annealed in situ (2 °C/min for the spine and 3 °C/min for the test plates) and in (D) spines were first annealed ex situ at 200, 250, 300, and 400 °C for 1 h, and second, transverse sections were obtained. The position of the beam through the sample during measurement is symbolized by a white dot on the sample's photographs. The hexagonal dashed lines indicate the orientation of the {*hk*0} planes. The SAXS intensities are displayed in a log scale (photograph G. Laurent, Sorbonne Université).

$$K \infty \frac{1}{(k_B T)} \exp\left(-\frac{E_a}{k_B T}\right) \tag{7}$$

Here, T is absolute temperature, k_B is the Boltzmann constant, and E_a is the activation energy of the diffusion process responsible for pore coarsening. The power index n depends on the diffusion path of point defects (vacancies) moving between the pores and thus mediating the coarsening.[64] Pore (or void) formation via vacancy diffusion was known after the discovery of the Kirkendall effect.[65] An important consequence followed from Kirkendall's diffusion mechanism is the presence of pores formed during diffusion.[66] These pores act as sinks for vacancies, and at some stage, vacancy accumulation become substantial and further expand via Ostwald ripening to reduce free energy of the system. The latter process is like the heat-mediated grain growth in polycrystals and precipitate growth in the binary (or multiphase) systems. In the case of bulk diffusion, n equals 3[67] and for surface diffusion (or diffusion along two-dimensional defects e.g., grain boundaries), $n = 4$.[64,68]

For isochronous annealing (equal time durations for each temperature), using eqs 6 and 7 leads to the following expression for the growth of the average pore radius with increasing temperature:

$$R_a^n(T + \Delta T) - R_a^n(T) = A \frac{1}{(k_B T)} \exp\left(-\frac{E_a}{k_B T}\right) \tag{8}$$

where ΔT is the temperature increment and A is some temperature-independent constant (proportional to the time-step duration in the isochronous experiment).

Using experimental data for gyration radii (Figure 7A), we can plot the increments, $R_g^n(T + \Delta T) - R_g^n(T)$, as a function of temperature (Figures SI3D and 7C). Since thermodynamic theories of Ostwald ripening require conservation of the total pore volume, the fittings of experimental data to eq 8 were performed for the increasing parts of $R_g^n(T + \Delta T) - R_g^n(T)$, i.e., up to 250 °C for the spines and up to 370 °C for the test plates (see Figure SI3D for more details).

Best fits of experimental data to eq 8 are shown in Figure 7C. For dense spines (composed mainly of imperforate stereoms), successful fitting requires $n = 3$ and provides an activation energy, $E_a = 2.61$ eV, which is close to $E = 2.81$ eV, the latter being characteristic for bulk self-diffusion of Ca in calcite.[69] In contrast, for the macroporous test plates, the best fit is obtained for $n = 4$ and the resulting $E_a = 1.0$ eV is almost three times lower than that for the spines, indicating that the nanopore evolution is governed by surface diffusion near the pore/calcite interfaces rather than classical bulk diffusion.

In addition, dissimilar levels of microporosity in the test plates and the spines are observed at 450 °C (Figure 7C). It appears that the high pore density in the test plates exceeds some "percolation threshold", which makes surface diffusion a leading factor in pore evolution. In contrast, pore density in the spines is well below this "percolation threshold" and therefore the respective activation energy is only slightly lower than that for bulk diffusion in pure calcite. Therefore, we suggest that pore

https://doi.org/10.1021/acs.cgd.2c00083
Cryst. Growth Des. 2022, 22, 3727−3739

coarsening in sea urchin skeletal elements is regulated either by surface or bulk diffusion depending on the specimens' macroporosity and possibly the microinternal interfaces.

3.4. Organic−Inorganic Interfaces. Organic−inorganic interfaces in biominerals are of great importance to the improved mechanical properties of the latter since they facilitate or hamper crack propagation. In this context, the interface orientation regarding the main crystallographic directions in calcite is especially important. Here, we used the 2D SAXS patterns collected at different temperatures to determine the orientation of the internal organic-inorganic interfaces with respect to the calcite *c*-axis. Note that electron density of calcite (0.815 e/Å^3) is almost twice that of intracrystalline organics (0.42 e/Å^3)[70] giving an orientation-dependent contrast in SAXS measurements. Above 250 °C, the contrast is further enhanced after ACC crystallization and organics removal.

At the native state (25 °C), the test plates and the spines show anisotropic elongated diffuse scattering signals along the *c*-axis when measured with their *c*-axis perpendicular to the X-ray beam (Figures 8A,C and SI1A,D). However, when measured with their *c*-axis parallel to the beam, both samples present isotropic 2D SAXS patterns (Figure 8B,D). Above 200 °C for the spines and 300 °C for the test plates, the SAXS signals show striking modifications (Figure 8) as described below.

In the test plates, the scattered intensity for both orientations increases between 250 and 300 °C, i.e., when ACC crystallization is complete (Figure 8A).[38] Above 400 °C and clearly at 450 °C, the diffuse scattering shows a streak in the [001] direction for the sample oriented with its *c*-axis perpendicular to the beam. When the *c*-axis is aligned with the X-ray beam, a hexagonal-like pattern of diffuse scattering is measured, reflecting the basal symmetry of calcite. These SAXS signals originate from flat interfaces formed after the removal of organic macromolecules. Their orientation therefore provides information on the preferential localization of the organic molecules, which form organic-inorganic interfaces in the pristine biominerals. Thus, in the test plates, these molecules are preferentially localized perpendicular and along the *c*-axis in agreement with previous work.[38,46,71]

In the spines, the scattered intensity for both orientations increases at 200 °C, i.e., when ACC crystallization is maximal and before the maximum level of organics degradation (Figure 8A). For the sample oriented with its *c*-axis perpendicular to the beam, weak streaks in the [001] and [104] directions appear at 250 °C. The [104] streak, similar to that previously observed in *Pinna nobilis* mollusk shells[71] likely originates in the calcite cleavage planes. The appearance of the streak in the [104] direction is strongly dependent on the alignment of the sample with respect to the beam. Indeed, it was not observed in few other measurements (not shown). Therefore, we tested the appearance of the [104] streak in a sample that was preheated at 400 °C for 1 h and then sectioned at 45° with respect to the *c*-axis, which corresponds to the angle between the [104] and [001] vectors in reciprocal space. In this orientation, the streak is clearly seen along the [104] direction (Figure SI1E). The intensity of both the [001] and [104] streaks increases above 300 °C; however, above 400 °C only the intensity of the [001] streak increases further. Thus, the [104] streak likely results from the ACC crystallization into calcite, producing microcracks along the cleavage planes, whereas the [001] streak originates from flat organic−inorganic interfaces preferentially oriented perpendicular to the *c*-axis.

When the calcite *c*-axis of the spines is aligned with the X-ray beam, hexagonal-like SAXS patterns are observed in the temperature range from 250 to 400 °C. For the 400 °C annealed spine, a streak is also observed in one of the basal plane crystallographic directions (Figure 8D). The appearance of this streak is also very sensitive to the orientation of the sample with respect to the X-ray beam. As already mentioned, these features likely originate from the flat interfaces situated along the *c*-axis and likely formed after degradation of organic macromolecules initially localized on the respective planes.

To further characterize the interfaces responsible for the appearance of the [001] streaks at high temperatures, we analyzed the streak following ref 57 (see the Section 2 and Figures SI4 and SI5). This analysis allows determining the characteristic size, e.g., the radius of gyration (R_{fit}) of the scattering objects responsible for the streak appearance, as well as the angular spread, k_α, of the characteristic surfaces that form the objects (Figure SI5).

For the spines, the $I_{meas}(q_y)$ plots show Gaussian profiles with $k_{meas} \sim 0.02$ nm^{-1} and $\sqrt{k^2 + k_{res}^2} \sim 0.015$ nm^{-1}. In turn, the values of $\sqrt{k^2 + k_{res}^2}$ do not vary significantly between 340 and 450 °C, suggesting that $\sqrt{k^2 + k_{res}^2} \sim k_{res}$ and thus $k << k_{res}$ and $R_{fit} > 100$ nm. Therefore, above 340 °C, the elongated discontinuities like gaps in the calcite lattice outlined by flat surfaces that are produced by the removal of organic molecules are wider than 100 nm (the maximum size of the scattering objects measurable at the μSpot beamline[63]). In addition, a decrease in the angular spread, k_α, from 8 to 1° was measured with increasing temperature between 340 and 450 °C (Figure SI5), suggesting that the flat surfaces responsible for the [001] streak become better aligned (smoother) perpendicularly to the *c*-axis with rising temperatures.

For test plates, the $I_{meas}(q_y)$ profiles are broader than those in the spines, with $0.1 < k_{meas} < 0.2$ nm^{-1} (Figure SI5). The $\sqrt{k^2 + k_{res}^2}$ values decrease from 0.09 to 0.06 nm^{-1} with increasing temperatures from 400 to 450 °C. Taking $k_{res} = 0.015$ nm^{-1}, leads to 20 nm < R_{fit} < 30 nm. Finally, the angular spread also decreases with increasing temperatures (from 10 to 6°) suggesting that at 450 °C the gaps in the test plates also become better aligned but the effect is less pronounced than in spines.

4. CONCLUSIONS

Porosity is an essential part of biomineralization processes that involve amorphous particle attachment and subsequent crystallization. In this way, the system can tolerate the differences in the specific volumes of the amorphous and crystalline states, as well as related strains/stresses. In this study, we investigated the heat-induced evolution of internal interfaces in the skeletal elements—test plates and spines—of *P. lividus* sea urchins. These two biominerals exhibit different stereomic macrostructures, mainly galleried stereom comprising 5 to 10 μm sized pores for the test plates and compact septa (without macroporosity) for the spines. By using *in situ* heating synchrotron SAXS measurements, SEM, and FIB-SEM visualization techniques, we show that the kinetics and mechanisms of nano- and micro-pore evolution upon the crystallization of remnant ACC and the degradation of organic molecules, vary significantly between the two samples, in a manner that relates to their pristine macroporosity and internal organic-inorganic interfaces.

https://doi.org/10.1021/acs.cgd.2c00083
Cryst. Growth Des. 2022, 22, 3727−3739

The obtained results show the presence of nanopores, likely filled with hydrated organics in the pristine samples, and the coarsening of these nanopores with temperature. Coarsening follows the mechanisms predicted by classical Ostwald ripening, which is thermodynamically driven toward the reduction of surface contribution to free energy. The nanopore coarsening can be well described in the framework of the known thermodynamics-based theories, allowing the extraction of the activation energies, E_a, of the respective diffusion processes and power indices, n, for the growth of the pore radius with time. These parameters were found to be drastically different in the test plates and spines, being equal, respectively, to $n = 4$, $E_a = 1.0$ eV and $n = 3$, $E_a = 2.61$ eV. In other words, the nanopore evolution in the spines is controlled by bulk diffusion opposed to surface diffusion in the test plates.

In addition, the increase in size of the nanopores, which occurs mainly via coarsening in the test plates, starts at higher temperatures and is slower than in the spines where an additional increase of the total pore volume is also observed. We propose that the struts of the stereom are thin enough to compensate for volume shrinkage upon heating possibly via dilatation of the external surfaces whereas in the dense septa, an extra volume should be stored within the material's bulk. Moreover, the microporosity observed at higher temperatures is also very different, revealing smaller pores and much higher pore density in the test plates than in the spines. We assume that the micropore density in the test plates is high enough for allowing continuous vacancy pathways via surface diffusion. In contrast, in the spines, the micropore density is lower than such "percolation threshold" and pore evolution is predominantly controlled by bulk diffusion.

Overall, the obtained results shed new light on the processes involved in ACC crystallization in sea urchin biominerals, which allow for the growth of large single crystals of calcite with meshlike macrostructures. In particular, these processes lead to the formation of biominerals with nano-organic inclusions of different densities and distributions within different skeletal elements of the same species. Indeed, nanopore density in the test needs to be significantly high in order to allow for surface-mediated percolation of porosity. Moreover, our results suggest that *in vivo*, ACC crystallization proceeds as far as organics can serve as space-filling and accommodate for density changes caused by the amorphous to crystalline transformation. Beyond this point, crystallization is hindered and ACC is kinetically trapped within the biominerals. A better understanding of the atomic-level structure, the nano- and micro-architecture, and porosity of the final ceramic mineral phase will allow efficient harnessing of bioinspired design that can overcome the challenges imposed by the mineralization processes of macroporous and large single crystals through amorphous precursors.

■ ASSOCIATED CONTENT

Supporting Information

The Supporting Information is available free of charge at https://pubs.acs.org/doi/10.1021/acs.cgd.2c00083.

Synchrotron and laboratory SAXS measurements; synchrotron SAXS data analysis; SEM micrographs; CT data; and FIB-SEM data analysis (PDF)

■ AUTHOR INFORMATION

Corresponding Authors

Marie Albéric − *Laboratoire Chimie de la Matière Condensée de Paris, Sorbonne Université, Paris 75005, France;* orcid.org/0000-0002-5322-9904; Email: marie.alberic@sorbonne-universite.fr

Peter Fratzl − *Department of Biomaterials, Max Planck Institute of Colloids and Interfaces, Potsdam 14476, Germany;* Email: peter.fratzl@mpikg.mpg.de

Authors

Emil Zolotoyabko − *Department of Materials Science and Engineering, Technion-Israel Institute of Technology, Haifa 32000, Israel*

Oliver Spaeker − *Department of Biomaterials, Max Planck Institute of Colloids and Interfaces, Potsdam 14476, Germany;* orcid.org/0000-0002-4542-120X

Chenghao Li − *Department of Biomaterials, Max Planck Institute of Colloids and Interfaces, Potsdam 14476, Germany*

Maryam Tadayon − *Center for Molecular and Cellular Bioengineering, Technische Universität Dresden, Dresden 01307, Germany*

Clemens N.Z. Schmitt − *Department of Biomaterials, Max Planck Institute of Colloids and Interfaces, Potsdam 14476, Germany*

Yael Politi − *Center for Molecular and Cellular Bioengineering, Technische Universität Dresden, Dresden 01307, Germany;* orcid.org/0000-0002-2872-8277

Luca Bertinetti − *Center for Molecular and Cellular Bioengineering, Technische Universität Dresden, Dresden 01307, Germany;* orcid.org/0000-0002-4666-9610

Complete contact information is available at: https://pubs.acs.org/10.1021/acs.cgd.2c00083

Funding

M.A. was supported by an Alexander von Humboldt postdoctoral fellowship (ref 3.3-FRA-1163259-HFST-P). Open access funded by Max Planck Society.

Notes

The authors declare no competing financial interest.

■ ACKNOWLEDGMENTS

We are grateful to Birgit Schonert, Heike Runge, and Daniel Werner from MPI (Potsdam), respectively, for FIB-SEM sample preparation, SEM observations, and laboratory SAXS measurements. We thank Ernesto Scoppola and Wolfgang Wagermaier from MPI (Potsdam) for their help and discussion concerning the SAXS streak analysis. We thank Francisco Fernandes, Niki Baccile, Vaskar Sardhalia, and Guillaume Laurent from Sorbonne Université (Paris), respectively, for helping with FIJI software, discussion about the SAXS data analysis, performing extra laboratory SAXS measurements, and taking photographs of the samples. Finally, we acknowledge the Swiss Light Source for allocating beam time and the invaluable assistance of the beamline scientist Goran Lovric.

■ REFERENCES

(1) Meldrum, F. C.; Seshadri, R. Porous Gold Structures through Templating by Echinoid Skeletal Plates. *Chem. Commun.* **2000**, *1*, 29−30.

(2) Weber, J. N.; White, E. W.; Lebiedzik, J. New Porous Biomaterials by Replication of Echinoderm Skeletal Microstructures. *Nature* **1971**, *233*, 337−339.

(3) Park, R. J.; Meldrum, F. C. Synthesis of Single Crystals of Calcite with Complex Morphologies. *Adv. Mater.* **2002**, *14*, 1167−1169.
(4) Yue, W.; Park, R. J.; Kulak, A. N.; Meldrum, F. C. Macroporous Inorganic Solids from a Biomineral Template. *J. Cryst. Growth* **2006**, *294*, 69−77.
(5) Aizenberg, J.; Muller, D. A.; Grazul, J. L.; Hamann, D. R. Direct Fabrication of Large Micropatterned Single Crystals. *Science* **2003**, *299*, 1205.
(6) Aizenberg, J.; Hendler, G. Designing Efficient Microlens Arrays: Lessons from Nature. *J. Mater. Chem.* **2004**, *14*, 2066−2072.
(7) Yang, S.; Chen, G.; Megens, M.; Ullal, C. K.; Han, Y. J.; Rapaport, R.; Thomas, E. L.; Aizenberg, J. Functional Biomimetic Microlens Arrays with Integrated Pores. *Adv. Mater.* **2005**, *17*, 435−438.
(8) Lee, K.; Wagermaier, W.; Masic, A.; Kommareddy, K. P.; Bennet, M.; Manjubala, I.; Lee, S.-W.; Park, S. B.; Cölfen, H.; Fratzl, P. Self-Assembly of Amorphous Calcium Carbonate Microlens Arrays. *Nat. Commun.* **2012**, *3*, 725.
(9) Picker, A.; Nicoleau, L.; Burghard, Z.; Bill, J.; Zlotnikov, I.; Labbez, C.; Nonat, A.; Cölfen, H. Mesocrystalline Calcium Silicate Hydrate: A Bioinspired Route toward Elastic Concrete Materials. *Sci. Adv.* **2017**, *3*, No. e1701216.
(10) Heatfield, B. M.; Travis, D. F. Ultrastructural Studies of Regenerating Spines of the Sea Urchin Strongylocentrotus Purpuratus. *J. Morphol.* **1975**, *145*, 51−71.
(11) Markel, K.; Roser, U. The Spine Tissues in the Echinoid Eucidaris-Tribuloides. *Zoomorphology* **1983**, *103*, 25−41.
(12) Weber, J.; Greer, R.; Voight, B.; White, E.; Roy, R. Unusual Strength Properties of Echinoderm Calcite Related to Structure. *J. Ultrastruct. Res.* **1969**, *26*, 355−366.
(13) Tsafnat, N.; Fitz Gerald, J. D.; Le, H. N.; Stachurski, Z. H. Micromechanics of Sea Urchin Spines. *PLoS One* **2012**, *7*, No. e44140.
(14) Aizenberg, J.; Tkachenko, A.; Weiner, S.; Addadi, L.; Hendler, G. Calcitic Microlenses as Part of the Photoreceptor System in Brittlestars. *Nature* **2001**, *412*, 819−822.
(15) Hendler, G.; Byrne, M. Fine-Structure of the Dorsal Arm Plate of Ophiocoma-Wendti - Evidence for a Photoreceptor System (Echinodermata, Ophiuroidea). *Zoomorphology* **1987**, *107*, 261−272.
(16) Raup, D. M. Crystallography of Echinoid Calcite. *J. Geol.* **1959**, *67*, 661−674.
(17) Donnay, G.; Pawson, D. L. X-Ray Diffraction Studies of Echinoderm Plates. *Science* **1969**, *166*, 1147−1150.
(18) Tsipursky, S. J.; Buseck, P. R. Structure of Magnesian Calcite from Sea Urchins. *Am. Mineral.* **1993**, *78*, 775−781.
(19) Larsson, A.-K.; Christy, A. G. On Twinning and Microstructures in Calcite and Dolomite. *Am. Mineral.* **2008**, *93*, 103−113.
(20) Addadi, L.; Raz, S.; Weiner, S. Taking Advantage of Disorder: Amorphous Calcium Carbonate and Its Roles in Biomineralization. *Adv. Mater.* **2003**, *15*, 959−970.
(21) Cölfen, H. Single Crystals with Complex Form via Amorphous Precursors. *Angew. Chem., Int. Ed.* **2008**, *47*, 2351−2353.
(22) Weiner, S.; Levi-Kalisman, Y.; Raz, S.; Addadi, L. Biologically Formed Amorphous Calcium Carbonate. *Connect Tissue Res.* **2003**, *44*, 214−218.
(23) Weber, E.; Pokroy, B. Intracrystalline Inclusions within Single Crystalline Hosts: From Biomineralization to Bio-Inspired Crystal Growth. *CrystEngComm* **2015**, *17*, 5873−5883.
(24) Zolotoyabko, E. Anisotropic Lattice Distortions in Biogenic Minerals Originated from Strong Atomic Interactions at Organic/Inorganic Interfaces. *Adv. Mater. Interfaces* **2017**, *4*, No. 1600189.
(25) Meldrum, F. C.; Ludwigs, S. Template-Directed Control of Crystal Morphologies. *Macromol. Biosci.* **2007**, *7*, 152−162.
(26) Fratzl, P.; Fischer, F. D.; Svoboda, J.; Aizenberg, J. A Kinetic Model of the Transformation of a Micropatterned Amorphous Precursor into a Porous Single Crystal. *Acta Biomater.* **2010**, *6*, 1001−1005.
(27) Jensen, A. C. S.; Imberti, S.; Parker, S. F.; Schneck, E.; Politi, Y.; Fratzl, P.; Bertinetti, L.; Habraken, W. J. E. M. Hydrogen Bonding in Amorphous Calcium Carbonate and Molecular Reorientation Induced by Dehydration. *J. Phys. Chem. C* **2018**, *122*, 3591−3598.
(28) Loste, E.; Park, R. J.; Warren, J.; Meldrum, F. C. Precipitation of Calcium Carbonate in Confinement. *Adv. Funct. Mater.* **2004**, *14*, 1211−1220.
(29) Cheng, X.; Gower, L. B. Molding Mineral within Microporous Hydrogels by a Polymer_Induced Liquid_Precursor (PILP) Process. *Biotechnol. Prog.* **2006**, *22*, 141.
(30) Kim, Y.-Y.; Douglas, E. P.; Gower, L. B. Patterning Inorganic (CaCO3) Thin Films via a Polymer-Induced Liquid-Precursor Process. *Langmuir* **2007**, *23*, 4862−4870.
(31) Tester, C. C.; Wu, C.-H.; Weigand, S.; Joester, D. Precipitation of ACC in Liposomes—a Model for Biomineralization in Confined Volumes. *Faraday Discuss.* **2012**, *159*, 345−356.
(32) Tester, C. C.; Whittaker, M. L.; Joester, D. Controlling Nucleation in Giant Liposomes. *Chem. Commun.* **2014**, *50*, 5619−5622.
(33) Gong, X.; Wang, Y.-W.; Ihli, J.; Kim, Y.-Y.; Li, S.; Walshaw, R.; Chen, L.; Meldrum, F. C. The Crystal Hotel: A Microfluidic Approach to Biomimetic Crystallization. *Adv. Mater.* **2015**, *27*, 7395−7400.
(34) Zeng, Y.; Cao, J.; Wang, Z.; Guo, J.; Zhou, Q.; Lu, J. Insights into the Confined Crystallization in Microfluidics of Amorphous Calcium Carbonate. *Cryst. Growth Des.* **2018**, *18*, 6538−6546.
(35) Li, S.; Zeng, M.; Gaule, T.; McPherson, M. J.; Meldrum, F. C. Passive Picoinjection Enables Controlled Crystallization in a Droplet Microfluidic Device. *Small* **2017**, *13*, No. 1702154.
(36) Cavanaugh, J.; Whittaker, M. L.; Joester, D. Crystallization Kinetics of Amorphous Calcium Carbonate in Confinement. *Chem. Sci.* **2019**, *10*, 5039−5043.
(37) Seto, J.; Ma, Y. R.; Davis, S. A.; Meldrum, F.; Gourrier, A.; Kim, Y. Y.; Schilde, U.; Sztucki, M.; Burghammer, M.; Maltsev, S.; Jäger, C.; Cölfen, H. Structure-Property Relationships of a Biological Mesocrystal in the Adult Sea Urchin Spine. *Proc. Natl. Acad. Sci. U. S. A.* **2012**, *109*, 3699−3704.
(38) Albéric, M.; Caspi, E. N.; Bennet, M.; Ajili, W.; Nassif, N.; Azaïs, T.; Berner, A.; Fratzl, P.; Zolotoyabko, E.; Bertinetti, L.; Politi, Y. Interplay between Calcite, Amorphous Calcium Carbonate, and Intracrystalline Organics in Sea Urchin Skeletal Elements. *Cryst. Growth Des.* **2018**, *18*, 2189−2201.
(39) Lauer, C.; Haußmann, S.; Schmidt, P.; Fischer, C.; Rapp, D.; Berthold, C.; Nickel, K. G. On the Relation of Amorphous Calcium Carbonate and the Macromechanical Properties of Sea Urchin Spines. *Adv. Eng. Mater.* **2020**, *22*, No. 1900922.
(40) Politi, Y.; Arad, T.; Klein, E.; Weiner, S.; Addadi, L. Sea Urchin Spine Calcite Forms via a Transient Amorphous Calcium Carbonate Phase. *Science* **2004**, *306*, 1161−1164.
(41) Albéric, M.; Stifler, C.; Zou, Z.; Sun, C.; Killian, C.; Valencia, S.; Mawass, M. A.; Bertinetti, L.; Gilbert, P. U. P. A.; Politi, Y. Growth an Regrowth of Adult Sea Urchin Psines Involve Hydrated and Anhydrous Amorphous Calcium Carbonate Precursors. *J. Struct. Biol.* **2019**, *1*, No. 100004.
(42) Politi, Y.; Metzler, R. A.; Abrecht, M.; Gilbert, B.; Wilt, F. H.; Sagi, I.; Addadi, L.; Weiner, S.; Gilbert, P. Transformation Mechanism of Amorphous Calcium Carbonate into Calcite in the Sea Urchin Larval Spicule. *Proc. Natl. Acad. Sci. U. S. A.* **2008**, *105*, 17362−17366.
(43) Gong, Y. U. T.; Killian, C. E.; Olson, I. C.; Appathurai, N. P.; Amasino, A. L.; Martin, M. C.; Holt, L. J.; Wilt, F. H.; Gilbert, P. U. P. A. Phase Transitions in Biogenic Amorphous Calcium Carbonate. *Proc. Natl. Acad. Sci. U. S. A.* **2012**, *109*, 6088−6093.
(44) Herman, A.; Addadi, L.; Weiner, S. Interactions of Sea-Urchin Skeleton Macromolecules with Growing Calcite Crystals - a Study of Intracrystalline Proteins. *Nature* **1988**, *331*, 546−548.
(45) Berman, A.; Addadi, L.; Kvick, A.; Leiserowitz, L.; Nelson, M.; Weiner, S. Intercalation of Sea Urchin Proteins in Calcite: Study of a Crystalline Composite Material. *Science* **1990**, *250*, 664−667.
(46) Aizenberg, J.; Hanson, J.; Koetzle, T. F.; Weiner, S.; Addadi, L. Control of Macromolecule Distribution within Synthetic and Biogenic Single Calcite Crystals. *J. Am. Chem. Soc.* **1997**, *119*, 881−886.
(47) Albeck, S.; Aizenberg, J.; Addadi, L.; Weiner, S. Interactions of Various Skeletal Intracrystalline Components with Calcite Crystals. *J. Am. Chem. Soc.* **1993**, *115*, 11691−11697.

https://doi.org/10.1021/acs.cgd.2c00083
Cryst. Growth Des. 2022, 22, 3727−3739

(48) Kanold, J. M.; Guichard, N.; Immel, F.; Plasseraud, L.; Corneillat, M.; Alcaraz, G.; Brümmer, F.; Marin, F. Spine and Test Skeletal Matrices of the Mediterranean Sea Urchin Arbacia Lixula - a Comparative Characterization of Their Sugar Signature. *FEBS J.* **2015**, *282*, 1891−1905.
(49) Su, X.; Kamat, S.; Heuer, A. H. The Structure of Sea Urchin Spines, Large Biogenic Single Crystals of Calcite. *J. Mater. Sci.* **2000**, *35*, 5545−5551.
(50) Kelm, K.; Goetz, A.; Sehrbrock, A.; Irsen, S. H.; Hoffmann, R.; Schmahl, W. W.; Griesshaber, E. Mosaic Structure in the Spines of Holopneustes Porossisimus. *Z. Kristallogr. Cryst. Mater.* **2012**, *227*, 758−765.
(51) Smith, L. C.; Hawley, T. S.; Henson, J. H.; Majeske, A. J.; Oren, M.; Rosental, B. Methods for Collection, Handling, and Analysis of Sea Urchin Coelomocytes. *Methods Cell Biol.* **2019**, *150*, 357−389.
(52) Glatter, O.; Kratky, O. *Small Angle X-Ray Scattering*; Academic Press; London, 1982.
(53) Fratzl, P.; Fratzl-Zelman, N.; Klaushofer, K.; Vogl, G.; Koller, K. Nucleation and Growth of Mineral Crystals in Bone Studied by Small-Angle X-Ray Scattering. *Calcif. Tissue Int.* **1991**, *48*, 407−413.
(54) Baur, R.; Gerold, V. Vergleichende Röntgenographische Und Elektronenmikroskopische Untersuchungen Der Grösse von Guinier-Preston-Zonen in Aluminium-Silber. *Acta Metall.* **1964**, *12*, 1449−1453.
(55) Benecke, G.; Wagermaier, W.; Li, C.; Schwartzkopf, M.; Flucke, G.; Hoerth, R.; Zizak, I.; Burghammer, M.; Metwalli, E.; Müller-Buschbaum, P.; Trebbin, M.; Förster, S.; Paris, O.; Roth, S.; Fratzl, P. A Customizable Software for Fast Reduction and Analysis of Large X-Ray Scattering Data Sets: Applications of the New DPDAK Package to Small-Angle X-Ray Scattering and Grazing-Incidence Small-Angle X-Ray Scattering. *J. Appl. Crystallogr.* **2014**, *47*, 1797−1803.
(56) Hammouda, B. A New Guinier−Porod Model. *J. Appl. Crystallogr.* **2010**, *43*, 716−719.
(57) Fratzl, P.; Langmayr, F.; Paris, O. Evaluation of 3D Small-Angle Scattering from Non-Spherical Particles in Single Crystals. *J. Appl. Crystallogr.* **1993**, *26*, 820−826.
(58) Ronneberger, O.; Fischer, P.; Brox, T. U-Net: Convolutional Networks for Biomedical Image Segmentation. In *Medical Image Computing and Computer-Assisted Intervention − MICCAI 2015*; Navab, N., Hornegger, J., Wells, W. M., Frangi, A. F., Eds.; Springer International Publishing: Cham, 2015; 234−241.
(59) Smith, B. A. Stereom Microstructure of the Echinoid Test. *Special Papers in Palaeontology* 1980, *25*, 1−324.
(60) Wynblatt, P.; Chatain, D. Effects of Anisotropy on the Equilibrium Shape of Nanoscale Pores at Grain Boundaries. *Acta Mater.* **2013**, *61*, 4572−4580.
(61) Gorzelak, P.; Dery, A.; Dubois, P.; Stolarski, J. Sea Urchin Growth Dynamics at Microstructural Length Scale Revealed by Mn-Labeling and Cathodoluminescence Imaging. *Front. Zool.* **2017**, *14*, 42.
(62) Voorhees, P. W. The Theory of Ostwald Ripening. *J. Statist. Phys.* **1985**, *38*, 231−252.
(63) Paris, O.; Li, C.; Siegel, S.; Weseloh, G.; Emmerling, F.; Riesemeier, H.; Erko, A.; Fratzl, P. A New Experimental Station for Simultaneous X-Ray Microbeam Scanning for Small- and Wide-Angle Scattering and Fluorescence at BESSY II. *J. Appl. Crystallogr.* **2007**, *40*, s466−s470.
(64) Vengrenovitch, R. D. On the Ostwald Ripening Theory. *Acta Metall.* **1982**, *30*, 1079−1086.
(65) Smigelskas, A. D.; Kirkendall, E. O. Zinc Diffusion in Alpha Brass. *Trans. AIME* **1947**, *171*, 130−142.
(66) Seitz, F. On the Porosity Observed in the Kirkendall Effect. *Acta Metall.* **1953**, *1*, 355−369.
(67) Lifshitz, I. M.; Slyozov, V. V. The Kinetics of Precipitation from Supersaturated Solid Solutions. *J. Phys. Chem. Solids* **1961**, *19*, 35−50.
(68) Speight, M. V. Growth Kinetics of Grain-Boundary Precipitates. *Acta Metall.* **1968**, *16*, 133−135.
(69) Fisler, D. K.; Cygan, R. T. Diffusion of Ca and Mg in Calcite. *Am. Mineral.* **1999**, *84*, 1392−1399.
(70) Younis, S.; Kauffmann, Y.; Bloch, L.; Zolotoyabko, E. Inhomogeneity of Nacre Lamellae on the Nanometer Length Scale. *Cryst. Growth Des.* **2012**, *12*, 4574−4579.
(71) Gilow, C.; Zolotoyabko, E.; Paris, O.; Fratzl, P.; Aichmayer, B. Nanostructure of Biogenic Calcite Crystals: A View by Small-Angle X-Ray Scattering. *Cryst. Growth Des.* **2011**, *11*, 2054−2058.

https://doi.org/10.1021/acs.cgd.2c00083
Cryst. Growth Des. 2022, 22, 3727−3739